High-throughput computational screening of Heusler compounds with phonon considerations for enhanced material discovery

Enda Xiao*
Research Center for Magnetic and Spintronic Materials, National Institute for Materials Science, 1-2-1 Sengen, Tsukuba, 305-0047, Ibaraki, Japan

Terumasa Tadano†
Research Center for Magnetic and Spintronic Materials, National Institute for Materials Science, 1-2-1 Sengen, Tsukuba, 305-0047, Ibaraki, Japan and Digital Transformation Initiative Center for Magnetic Materials (DXMag), National Institute for Materials Science, 1-2-1 Sengen, Tsukuba, 305-0047, Ibaraki, Japan

(Dated: September 10, 2025)

High-throughput (HTP) *ab initio* calculations are performed on 27,865 Heusler compositions, covering a broad range of regular, inverse, and half-Heusler compounds in both cubic and tetragonal phases. In addition to conventional stability metrics, such as formation energy, Hull distance, and magnetic critical temperature T_c, phonon stability is assessed by systematically conducting *ab initio* phonon calculations for over 8,000 compounds. The performance of *ab initio* stability criteria is systematically assessed against 189 experimentally synthesized compounds, and magnetic critical temperature calculations are validated using 59 experimental data points. As a result, we identify 631 stable compounds as promising candidates for further functional material exploration. Notably, 47 low-moment ferrimagnets are identified, with their spin polarization and anomalous Hall/Nernst conductivity calculated to provide insights into potential applications in spintronics and energy harvesting. Furthermore, our analyses reveal linear relationship between T_c and magnetization in 14 systems and correlations between stability and atomic properties such as atomic radius and ionization energy. The regular/inverse structures preference in X_2YZ compound and tetragonal distortion are also investigated for a broad Heusler family.

I. INTRODUCTION

Heusler alloys are renowned for their exceptional magnetic and functional properties, including high-saturation magnetization, substantial magnetocrystalline anisotropy (MCA), elevated magnetic critical temperature (T_c), significant magnetocaloric effects, and notable thermoelectric performance [1]. The unique combination of these properties, along with the diverse compositions within the Heusler family, has prompted extensive high-throughput (HTP) studies to explore their potential for various applications [2–11]. Previous HTP investigations have primarily relied on stable compounds in various databases, such as the Heusler database at the University of Alabama, the Open Quantum Materials Database (OQMD), and the AFLOW database [9, 12, 13]. However, these databases are limited in the scope of the Heusler compound family, restricting the exploration of functional material candidates.

In HTP studies, the initial candidate pool is typically narrowed by assessing the thermodynamic stability of compounds. Thermodynamic stability is commonly evaluated using formation energy and distance to the convex hull, which quantify stability relative to its decomposition into constituent elements or competing phases. However, the consideration of dynamical stability, ensuring that a compound does not undergo structural phase transitions, is rarely incorporated into HTP frameworks due to the computational cost and complexity of phonon calculations in magnetic systems.

Since most of the intriguing properties of Heusler compounds are related to magnetism, it is vital to ensure the thermal stability of their magnetic configurations at application temperatures. This stability is typically assessed using T_c. Previous studies have estimated T_c using linear interpolation derived from experimental data [6, 14–16]. Some efforts have also employed mean-field theory combined with exchange interaction constants from first-principles calculations to estimate T_c [17, 18]. However, the reliability and accuracy of T_c calculations have not been thoroughly investigated against experimental results in a comprehensive Heusler space.

The diversity of Heusler compounds arises not only from their composition but also from the possible structures they can adopt for a given composition. Heusler compounds with the X_2YZ composition can typically crystallize in either regular or inverse structures, assuming no chemical disorder. An empirical rule of structural preference in X_2YZ Heusler compounds, referred to as Burch's rule in some studies, has been employed in various works [18–22]. While this rule has slightly different descriptions in different works, the key point is that the inverse structure is preferred when the Y element is located to the right of the X element in the periodic table, and vice versa. This empirical rule has been validated by HTP *ab initio* studies containing a few hundred com-

* Xiao.Enda@nims.go.jp
† Tadano.Terumasa@nims.go.jp

pounds [18, 22], but its validity for a broader compositional space is not clarified. Besides, Heusler compounds typically crystallize in the cubic or tetragonal phase. The tetragonal phase, also referred to as tetragonal distortion, is essential for a material to exhibit MCA, which is particularly critical for developing materials with strong perpendicular magnetic anisotropy (PMA) [23].

Recently, Heusler alloys have also emerged as promising candidates for compensated ferrimagnet (CFiM) systems. Compared to traditional ferromagnetic (FM) materials, CFiM offers several advantages for spintronics applications due to its low moment, such as faster switching speeds, higher storage densities, and greater resistance to external magnetic fields. [24]. Notably, CFiM systems have inequivalent magnetic sublattices, enabling conventional electrical reading and writing mechanisms on FM systems, such as anomalous Hall effect (AHE), tunnel magnetoresistance (TMR), spin-transfer torque (STT), and spin-orbit torque (SOT) [24]. However, only a few Mn-contained CFiM Heusler compounds have been synthesized and investigated [25–34]. CFiM can be obtained from low-moment ferrimagnet (FiM) by adjusting the chemical composition and concentration. Thus, a low magnetic moment FiM are potential candidates for CFiM, but only a few systems have been proposed by first-principles calculation [35–39]. Thus, an expanded list of candidates taking stability into account is desired.

In this work, we conducted a HTP *ab initio* search for stable Heusler compounds covering a broad range of regular, inverse, and half structures in both cubic and tetragonal phases, significantly expanding the pool of materials available for functional exploration. Stability was assessed using conventional metrics such as formation energy, hull distance, and magnetic transition temperature. Additionally, we incorporated phonon stability, a critical factor omitted in previous high-throughput investigations. To confirm the validity of our screening and modeling procedure, we benchmarked the proposed stability criteria against a dataset of 189 experimentally synthesized compounds and the employed T_c calculation methods against 59 experimental data points. This comprehensive analysis identified 631 compounds that satisfy all stability criteria, marking them as promising candidates for further functional material exploration. Notably, we identified 47 low-moment FiM systems that meet all stability criteria. For these systems, we calculated the spin polarization (SP), anomalous Hall conductivity (AHC), and anomalous Nernst conductivity (ANC), providing insights into their potential applications in spintronics and energy harvesting devices.

Our comprehensive HTP result also revealed significant linear relationships between T_c and magnetization in 14 systems. We also observed correlations between compound stability and fundamental atomic properties such as atomic radius and ionization energy. Additionally, we confirmed that inverse Heusler compounds generally exhibit a lower electronegativity for the X element compared to the Y element, alongside a comparable covalent radius difference between these elements. Finally, we confirmed that tetragonal distortion correlates with a high density of states at the Fermi level in the cubic phase for X_2YZ compounds. We also found that this correlation extends to the studied half-Heusler compounds.

II. METHODOLOGY

A. Composition and structure

This HTP study investigates an extensive set of conventional Heusler compounds, as illustrated in Fig. 1 (a). The regular and inverse Heusler compounds share the X_2YZ composition, while half-Heusler compounds adopt the XYZ composition. The regular and inverse structures are identical when the X and Y elements are the same, resulting in an X_3Z composition. We considered all combinations of elements where X and Y are transition metals from the d-block (excluding Tc and Hg), and Z is a main group element from groups 13, 14, or 15 in the p-block, as depicted in Fig. 1 (a). For the X element, we additionally considered La and Lu, whose 4f orbitals are empty or fully occupied. This comprehensive screening resulted in a total of 27,864 compounds, including 9,072 regular, 9,072 inverse, 9,396 half-Heusler compounds, and 324 X_3Z compounds.

For regular and inverse Heusler compounds, the cubic regular structure belongs to the Fm$\bar{3}$m space group, with the X, Y, and Z atoms occupying the 8c ($\frac{1}{4},\frac{1}{4},\frac{1}{4}$), 4b ($\frac{1}{2},\frac{1}{2},\frac{1}{2}$), and 4a $(0,0,0)$ Wyckoff positions, respectively. The cubic inverse structure belongs to the Fm$\bar{4}$3m space group, with the X_1, X_2, Y, and Z atoms at 4c ($\frac{1}{4},\frac{1}{4},\frac{1}{4}$), 4b ($\frac{1}{2},\frac{1}{2},\frac{1}{2}$), 4d ($\frac{3}{4},\frac{3}{4},\frac{3}{4}$), and 4a $(0,0,0)$ Wyckoff positions, respectively. Half-Heusler compounds with XYZ composition adopt the cubic Fm$\bar{4}$3m space group, where the X, Y, and Z atoms occupy the 4c ($\frac{1}{4},\frac{1}{4},\frac{1}{4}$), 4b ($\frac{1}{2},\frac{1}{2},\frac{1}{2}$), and 4a $(0,0,0)$ Wyckoff positions, respectively. The tetragonal variants of regular, inverse, and half-Heusler structures belong to the I4/mmm, I$\bar{4}$m2, and I$\bar{4}$m2 space groups for regular, inverse, and half structures, respectively.

B. Workflow for high-throughput calculation

The workflow of the high-throughput *ab initio* calculation is schematically shown in Fig. 1(b), which we elaborate below.

a. Cell parameter optimization The initial structures of cubic Heuslers X_2YZ (or XYZ) were generated using a primitive cell containing one formula unit, where the initial lattice constant, a_{ini}, was set to the value reported in the OQMD for the same Heusler if available. When an OQMD calculated result was not available for X_2YZ (or XYZ), the corresponding a_{ini} value was estimated by simply taking the average of the a values of the OQMD-calculated Heuslers X_2YZ' (or XYZ') that

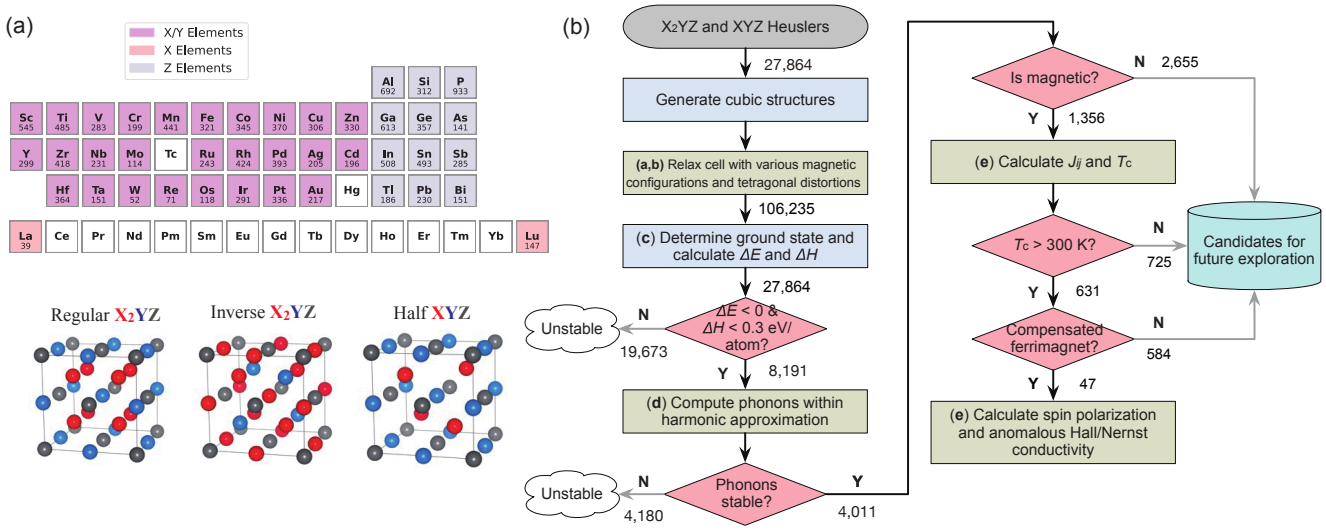

FIG. 1. (a) The compositions covered in the high-throughput search and distribution of stable compositions. Under each element, the number of compounds that contain this element and meet the stability criteria ($\Delta E < 0.0$ eV/atom and $\Delta H < 0.3$ eV/atom, and $\omega_{min} = 0$) is shown. (b) Workflow of the high-throughput search for stable Heusler compounds.

share the same X and Y elements. The cell parameters were then optimized by using the Vienna *ab initio* Simulation Package (VASP) [40–42]. For each composition, we considered various initial magnetic configurations following Ref. [43]. Specifically, for the regular Heusler X_2YZ and half Heusler XYZ, the X-site magnetic moment can either be parallel or antiparallel to the Y-site magnetic moment. For each spin configuration, we tested two magnitudes for the local magnetic moment, i.e., $|\boldsymbol{m}_i| = 1$ and 4 μ_B, to explore potential high-spin and low-spin states. Hence, four initial magnetic configurations were considered. In the case of the inverse Heusler X_2YZ, the spin moments at the two X sites can be antiparallel, so we considered eight initial configurations in total. After the structure optimizations were finished, the final energies and magnetic moments were compared to identify inequivalent (meta) stable states.

b. Tetragonal distortion For each inequivalent (meta) stable magnetic state identified, the cubic primitive cell was converted into a conventional cell containing two formula units, and the c-axis length was changed from its original value by ±2%, ±10%, +30%, and +50%. The cell parameters were then optimized further from these initial structures using VASP to explore potential lower-energy tetragonal phases. After the optimization, the structure with the lowest energy was identified as the ground state for the composition X_2YZ (or XYZ).

c. Thermodynamic stability For a compound to be stable against decomposition into its constituent elements, the formation energy (ΔE) must be negative. In addition, a compound is considered thermodynamically stable if its energy is lower than that of all possible competing phases. This relative stability can be evaluated by the distance to the convex hull (ΔH), and only compounds on the convex hull ($\Delta H = 0$) are thermodynamically stable in the strict sense. However, it is possible that metastable phases ($H > 0$) at zero Kelvin become most stable at finite temperatures or under external strain. Indeed, previous studies reported that many metastable compounds had been synthesized experimentally as long as H is reasonably small [44]. Hence, we relax the criterion and assume compounds to be thermodynamically stable if $\Delta H < 0.3$ eV/atom, which was chosen based on the analysis in the previous work. This choice is reasonable also for the Heuslers, as we will demonstrate below. To summarize, compounds satisfying both $\Delta E < 0.0$ eV/atom and $\Delta H < 0.3$ eV/atom were deemed thermodynamically stable and subject to dynamical stability analysis.

d. Dynamical stability For assessing the dynamical stability of Heuslers, phonon calculations were conducted within harmonic approximation using the ALAMODE package [45, 46]. The dynamical stability was assessed based on the presence/absence of unstable phonon modes on the $\boldsymbol{q}$ points commensurate with the supercell size. In this work, a $2\sqrt{2} \times 2\sqrt{2} \times 2$ conventional cell containing 32 formula units was employed; hence, there are 32 commensurate $\boldsymbol{q}$ points in the first Brillouin zone (BZ). If any of the eigenvalues of the dynamical matrix, i.e., the squared phonon frequencies $\{\omega^2_{\boldsymbol{q}\nu}\}$, were negative at the commensurate $\boldsymbol{q}$ points, the compound was assessed to be dynamically unstable. If all $\omega^2_{\boldsymbol{q}\nu}$ values were nonnegative, the compound was assumed to be dynamically stable and subject to the subsequent property calculations.

e. Property calculations The dynamically stable compounds were further split into magnetic and nonmagnetic systems. If the absolute sum of local magnetic moment per formula unit, $\sum_i |\boldsymbol{m}_i|$, is larger than 0.1 μ_B, the

system was considered magnetic. For the magnetic systems, the T_c was evaluated using the spin-polarized relativistic Korringa-Kohn-Rostoker (SPRKKR) code [47], and compounds having T_c higher than 300 K were identified. Among them, we identified compounds that simultaneously satisfy $\sum_i |\boldsymbol{m}_i| > 0.5\ \mu_B$ and $|\sum_i \boldsymbol{m}_i| < 0.5\ \mu_B$ as CFiM candidates, for which the ANC and AHC were computed systematically by using Wannier90 [48, 49].

C. Computational methods

Density functional theory (DFT) calculations were mainly conducted using VASP [40, 50]. The projector augmented wave method and the generalized gradient approximation (GGA) with the Perdew-Burke-Ernzerhof (PBE) functional were used [41, 42]. A plane-wave energy cutoff of 520 eV was applied, and the BZ was sampled using an automatically generated $\boldsymbol{k}$-point mesh by setting KSPACING=0.2 Å^{-1} except for the body-centered tetragonal (bct) lattice; for the bct lattice, the $\boldsymbol{k}$-mesh was generated using the Python Materials Genomics (pymatgen) library with a reciprocal density of 450 Å^3. The Methfessel-Paxton smearing [51] with widths of 0.05 eV and 0.1 eV was employed for structural optimization and phonon calculations, respectively. For electron density of states (DOS) calculations, the primitive cell was used and $\boldsymbol{k}$-mesh was generated using pymatgen with a denser density of 1000 Å^3, and the tetrahedron method with the Blöchl corrections was used [52].

The formation energy (ΔE) was calculated as the energy difference between the Heusler compound and its elemental constituents. The most stable elemental reference structures were obtained from the OQMD and then relaxed by VASP further using the DFT parameters described above to obtain the energies of the elemental constituents. The ΔH values were calculated using the formation energies computed for the Heuslers and those of the competing phases obtained from the OQMD (ver. 1.6). The HTP optimization scripts utilized the pymatgen package to generate input files for different initial structures using recommended pseudopotentials [53, 54]. Also, the Atomic Simulation Environment (ASE) toolkit [55] and the spglib [56] were employed for the structure file manipulation and symmetry analysis, respectively.

The phonon calculations were performed based on the supercell approach, as implemented in ALAMODE. Each atom in the supercell was displaced from its equilibrium position by 0.01–0.02 Å, and the atomic forces in the displaced configurations were computed using VASP. The second-order interatomic force constants (IFCs) between the atoms in the supercell were fitted to the displacement-force dataset, and the dynamical matrix was constructed from the IFCs to obtain the phonon frequencies. Phonon calculations for magnetic systems pose unique challenges, as small atomic displacements can alter the magnetic configuration in certain compounds. To circumvent this issue, we employed a two-step approach. First, a static DFT calculation was performed for the supercell without displacing atoms, and the resulting charge density was saved. Second, the DFT calculations for the displaced configurations were performed using the charge density obtained in the first step as initial values. Here, we also fixed the total magnetic moment to the desired value, as implemented by the NUPDOWN tag in VASP. We confirmed that this approach resulted in consistent magnetic moments for the displaced configurations in almost all cases. In-house scripts were employed for high-throughput phonon computations.

The T_c values were determined within the mean-field approximation using the exchange interaction constants J_{ij} [57]:

$$T_C = \frac{2}{3k_B} J_{\max}, \tag{1}$$

where $J_{\max}$ denotes the largest eigenvalue of the $J^{\mu\nu}$ matrix defined as $J^{\mu\nu} = \sum_{j\in\nu} J_{0j}$. Here, the index 0 is a fixed site in sublattice μ, and the summation runs over all sites in sublattice ν. J_{ij} values were calculated using the Liechtenstein formula, implemented in SPRKKR [58]. The exchange-correlation effects were treated within the PBE functional. The optimized structures by the VASP calculations were employed, and the local magnetic moments $\{m_i\}$ from the VASP calculations were used as the initial values. We confirmed overall consistency between the $\{m_i\}$ values obtained using SPRKKR and VASP, as shown in Fig. S2 in Supplemental Materials. The $\boldsymbol{k}$-point mesh for the self-consistent and J_{ij} calculations was $28 \times 28 \times 28$, and the basis set NL was set to 4. The cutoff radius flag CLURAD was set to 5 in the J_{ij} calculation, with which we confirmed convergence in T_c. Results employing the atomic sphere approximation (ASA) or full-potential (FP) method were computed [59]. The HTP T_c calculation scripts utilized the ASE2SPRKKR package to generate input files from the optimized structures [60, 61].

The anomalous Hall conductivity (σ_{xy}) was calculated using the Kubo formula in terms of the Berry curvature, as implemented in the Wannier90:

$$\sigma_{xy} = -\frac{e^2}{\hbar} \int_{\mathrm{BZ}} \frac{d\boldsymbol{k}}{(2\pi)^3} \sum_n f\left(\epsilon_{nk}\right) \Omega_{n,xy}(\boldsymbol{k}), \tag{2}$$

where $\hbar, e,\ \epsilon_{nk},\ f$, and $\Omega_{n,xy}$ represent the reduced Planck constant, positive elementary charge, eigenenergy, Fermi distribution, and Berry curvature, respectively. The Berry curvature is defined as

$$\Omega_{n,xy}(\boldsymbol{k}) = -2\hbar^2\, \mathrm{Im} \sum_{m(\neq n)} \frac{\langle n\boldsymbol{k}|\hat{v}_x|m\boldsymbol{k}\rangle\langle m\boldsymbol{k}|\hat{v}_y|n\boldsymbol{k}\rangle}{\left(\epsilon_{n\boldsymbol{k}} - \epsilon_{m\boldsymbol{k}}\right)^2}, \tag{3}$$

with $\hat{v}_x\,(\hat{v}_y)$ being the $k_x\,(k_y)$ component of the velocity operator, and $|nk\rangle$ representing the eigenstate. From the DFT band structure, Wannier functions were generated using the selected columns of the density matrix

(SCDM) method [62, 63]. The anomalous Nernst conductivity (α_{xy}) at finite temperature T was calculated from the energy-dependent anomalous Hall conductivity $\sigma_{xy}(\epsilon)$[64, 65]:

$$\alpha_{xy}(T) = \frac{1}{eT}\int d\epsilon\ (\epsilon - \mu)\frac{\partial f(\epsilon, T)}{\partial \epsilon}\sigma_{xy}(\epsilon, T = 0) \quad (4)$$

where μ is chemical potential and set to Fermi energy in the calculation. To realize integrations over the BZ in σ_{xy} calculation, a $\boldsymbol{k}$-mesh of $150 \times 150 \times 150$ points was used. The α_{xy} values were evaluated using $\sigma_{xy}(\epsilon)$ within a 0.8 eV energy window around the Fermi energy.

III. RESULTS

After relaxation, a total of 106,235 structures were identified, comprising 27,864 ground states and 78,371 metastable states. The stability of the ground states was further evaluated. Among these ground states, 8,191 (29.4%) satisfied the thermodynamic stability criteria of $\Delta E < 0.0$ eV/atom and $\Delta H < 0.3$ eV/atom. For the 8,191 screened compounds, we attempted *ab initio* phonon calculations and successfully obtained phonon frequencies for 8,180 compounds. For the remaining 11 cases, the phonon calculation results were not successful nor reliable either due to a convergence issue in DFT calculations or a large fitting error in the force constant estimation. Hence, these compounds were excluded from the subsequent calculations. Out of the 8,180 phonon computed compounds, 4,011 (14.4%) were identified dynamically stable, which include 1,898 regular, 1,192 inverse, 81 X_3Z, and 840 half-Heusler compounds. These findings underscore the importance of incorporating comprehensive stability metrics for efficient material discovery, highlighting that phonon stability can significantly narrow the candidates' list. In Fig. 1(a), the number of compounds that contain the corresponding element and meet the stability criteria is shown under each element.

For magnetic applications, it is essential that compounds exhibit a magnetic configuration that is stable at operational temperatures, typically room temperature. Among thermodynamically and dynamically stable compounds, 1,356 compounds have been identified as magnetic satisfying $\sum_{i\in\text{cell}} |\boldsymbol{m}_i| > 0.1\ \mu_\text{B}$. Of these, 631 compounds have a T_c exceeding 300 K, including 240 regular, 291 inverse, 24 X_3Z, and 76 half-Heusler structures. The FP T_c corrected by a factor of 0.85 were used. The validation of T_c calculation method is included in subsection IV A. The full list of stable magnetic compounds is included in the Supplemental Material.

Among the stable compounds, 47 low-moment FiM systems are identified, characterized by a total magnetization $|\boldsymbol{m}_\text{tot}| = |\sum_{i\in\text{cell}} \boldsymbol{m}_i|$ smaller than 0.5 μ_B and $\sum_{i\in\text{cell}} |\boldsymbol{m}_i|$ larger than 0.5 μ_B. These systems are listed in Table I. In previous work, it was proposed that compounds containing 24/18 valence electrons for X_2YZ/XYZ composition and Mn element are promising candidates, and several such compounds were found by first-principle calculations [35–37]. Our finding expands the list of low-moment Mn-containing compounds. We also find that Cr-containing compounds Cr_2YZ (Y=Pd, Pt, Rh) can also exhibit low moments. Two V-containing compounds and a Ti-containing compound are also identified. It should be noted that the Slater-Pauling rule is not valid for some compounds, while the valence electron number is close to the magic number 24 or 18. As suggested by the appearance of MnCrAs compound, we expect that quaternary type Heusler compounds containing Mn and Cr can exhibit small $|\boldsymbol{m}_\text{tot}|$ values, potentially providing more CFiM candidates.

To aid in the discovery of functional materials, we calculated the SP, AHC, and ANC to evaluate their potential performance, as listed in Table I. Notably, 17 compounds exhibit a SP greater than 0.6, which corresponds to a TMR of 112% according to the Jullière's formula [66]. Among these, Cr_2MnAs, MnCrAs, Mn_2OsGe, Ti_2CrSn, and Cr_2IrAl stand out with the SP values of 0.85, 0.87, 0.89, 0.96, and 0.96, respectively. In a recent work, low-moment FiM compounds Ti_2MnZ (Z=Al, Ga) were reported to exhibit promising AHC (253/268 $\text{S}\,\text{cm}^{-1}$) and ANC at room temperature (1.31/0.94 $\text{A}\,\text{m}^{-1}\,\text{K}^{-1}$) by first-principle calculation [38, 39]. Among the newly identified compounds, 12 compounds exhibit an AHC exceeding $250\,\text{S}\,\text{cm}^{-1}$ and 8 compounds exhibit an ANC exceeding $1\,\text{A}\,\text{m}^{-1}\text{K}^{-1}$. Given that the Fermi level can shift with variations in chemical composition and concentration in tuning for CFiM, we also present the maximum AHC and ANC values within an energy window of 250 meV around the Fermi level, as detailed in Table I.

As an example of the identified functional CFiM compounds, we show the calculated electronic band structures with and without spin-orbit coupling, the energy-dependent AHC/ANC, and the phonon band structure of inverse Mn_2RhAl in Fig. 2. The AHC shows a small variance around the Fermi level, suggesting the potential that total magnetization can be tuned by doping without lowering its AHC. The structure is tetragonally distorted with $a = 5.43$ Å and $c = 7.30$ Å whose local magnetic moments are shown in Table I. This structure exhibits $\Delta E = -0.48\,\text{eV/atom}$ and $\Delta H = 0.07\,\text{eV/atom}$, indicating its potential synthesizability. The energy of the structure is 0.18 eV/atom lower than the most stable regular structure having the same chemical formula Mn_2RhAl. Also, the ΔH value is lower than those of the competing half Heuslers MnRhAl and RhMnAl by 0.60 and 0.43 eV/atom, respectively, suggesting the preferred stability in the inverse structure. We also found another metastable inverse Mn_2RhAl that is less stable than the identified CFiM candidate only by 0.006 eV/atom. This competing structure is slightly distorted with $a = 5.92$ Å and $c = 5.94$ Å, and its total magnetic moment is $1.90\,\mu_\text{B}$/cell, which are consistent with the previously reported theoretical value for the cubic inverse Mn_2RhAl [67]. Since the energy difference between the two inverse structures is small, experimental

TABLE I. List of stable ferrimagnets with a total magnetization smaller than 0.5 μ_B/f.u. and an absolute sum of local magnetic moment larger than 0.5 μ_B/f.u. The table provides the formation energy ΔE (eV/f.u.), distance to the convex hull ΔH (eV/f.u.), total magnetic moment $m_{\rm tot}$ (μ_B/f.u.), local magnetic moments $m_{\rm loc}$ (μ_B), and magnetic critical temperature $T_{\rm c}$ (K) computed using the full-potential approach. Additionally, it includes the spin polarization SP, and electron density of states DOS (states eV^{-1}f.u.$^{-1}$) at the Fermi level, anomalous Hall conductivity σ_{xy} (S/cm), anomalous Nernst conductivity α_{xy} (A/Km), and the maximum anomalous Hall/Nernst conductivity $\sigma_{xy}^{\rm max}/\alpha_{xy}^{\rm max}$ within an energy window of 250 meV around the Fermi level. In type column, r/i/h represents regular/inverse/half, and c/t represents cubic/tetragonal. For easier comparison, the total magnetic moment in units of emu/cm^3 and emu/g are also included in the full list of statble compouds in Supplemental Material.

composition	type	ΔE	ΔH	$m_{\rm tot}$	$m_{\rm loc}$	$T_{\rm c}$	SP	DOS	σ_{xy}	$\sigma_{xy}^{\rm max}$	α_{xy}	$\alpha_{xy}^{\rm max}$
Cr_2AuAl	it	−0.04	0.16	0.06	[−2.90, 2.99, 0.01, −0.01]	1932	0.52	3.28	−658.02	−718.50	0.42	−1.78
Cr_2IrAl	ic	−0.28	0.19	0.01	[−2.05, 2.11, 0.00, 0.00]	1310	0.96	6.10	−325.17	−603.50	−0.11	2.37
Cr_2IrGe	it	−0.10	0.11	0.29	[2.53, −2.38, 0.12, 0.00]	1292	0.16	6.08	14.02	663.00	1.51	2.06
Cr_2MnAs	rt	−0.03	0.10	0.03	[−1.42, −1.42, 2.83, 0.08]	760	0.85	4.81	342.97	689.58	0.83	−2.30
Cr_2NiGe	it	−0.05	0.14	0.01	[2.29, −2.30, 0.00, 0.00]	1557	0.81	5.14	52.53	199.49	−0.12	1.00
Cr_2PdAl	it	−0.16	0.29	0.10	[2.88, −2.83, −0.01, 0.01]	1802	0.26	4.89	129.35	385.71	0.13	−1.19
Cr_2PdAs	it	−0.03	0.17	0.21	[3.04, −2.92, 0.05, 0.02]	1518	0.02	3.91	−86.87	−390.94	0.42	−1.35
Cr_2PdGa	it	−0.11	0.22	0.10	[2.93, −2.87, 0.00, 0.00]	1813	0.12	5.02	65.30	66.14	0.21	−0.51
Cr_2PdGe	it	−0.08	0.19	0.04	[−2.80, 2.85, 0.00, 0.00]	1811	0.68	3.34	−55.15	−66.43	0.09	−0.58
Cr_2PdSn	it	−0.02	0.27	0.08	[−3.07, 3.15, 0.01, 0.00]	1759	0.57	2.94	−18.76	−69.87	0.19	0.43
Cr_2PtAl	it	−0.32	0.20	0.15	[2.78, −2.71, 0.01, 0.00]	1701	0.31	4.91	235.79	246.94	0.09	−1.04
Cr_2PtGa	it	−0.23	0.10	0.11	[2.84, −2.78, 0.02, 0.00]	1734	0.19	4.75	100.26	−266.89	0.09	−1.26
Cr_2PtGe	it	−0.16	0.08	0.05	[−2.72, 2.80, −0.03, 0.00]	1727	0.63	3.34	−149.56	−241.16	−0.57	1.17
Cr_2PtIn	it	−0.05	0.21	0.00	[3.15, −3.16, −0.01, 0.00]	1660	0.23	4.81	−47.10	176.52	0.11	−1.01
Cr_2PtSi	it	−0.27	0.18	0.01	[2.46, −2.52, 0.04, 0.00]	1633	0.68	4.02	58.57	321.61	0.34	1.08
Cr_2PtSn	it	−0.10	0.21	0.04	[−3.01, 3.07, −0.02, 0.00]	1754	0.61	2.83	−181.73	−186.59	0.12	0.45
Cr_2RhGe	it	−0.14	0.14	0.41	[2.66, −2.42, 0.13, 0.00]	1482	0.12	5.82	−280.10	−315.97	−1.20	−1.81
Cr_2RhSb	it	−0.04	0.21	0.03	[−2.83, 2.92, −0.06, 0.01]	1621	0.67	3.52	9.60	−136.89	0.14	1.59
Cr_2RhSn	it	−0.04	0.23	0.11	[2.95, −2.92, 0.05, 0.00]	1544	0.32	4.91	−185.02	−412.51	0.01	2.03
CrMnAs	hc	−0.04	0.14	0.00	[−2.50, 2.60, 0.00]	2244	0.61	2.82	5.41	202.19	0.32	0.89
Mn_2AgAl	ic	−0.02	0.17	0.33	[−3.08, 3.38, 0.03, 0.01]	1218	0.56	4.82	220.09	297.21	0.12	−1.22
Mn_2AuIn	it	−0.00	0.12	0.03	[3.61, −3.60, 0.00, 0.01]	782	0.11	5.45	−25.94	531.99	1.23	1.48
Mn_2CuAl	it	−0.18	0.01	0.20	[−2.56, 2.77, 0.00, −0.01]	1264	0.60	4.72	11.41	56.12	0.15	0.16
Mn_2CuGa	it	−0.11	0.00	0.35	[−2.75, 3.06, 0.02, 0.00]	1205	0.57	4.70	11.09	301.80	0.13	1.03
Mn_2Ge	ht	−0.04	0.09	0.00	[−2.27, 2.36, −0.04]	1751	0.69	3.28	9.30	119.51	−0.20	−0.36
Mn_2IrAl	it	−0.51	0.00	0.22	[−2.81, 3.04, −0.01, 0.00]	947	0.38	5.27	−846.32	−969.32	−0.91	−1.44
Mn_2IrGa	it	−0.39	0.00	0.20	[−2.93, 3.13, −0.02, 0.01]	984	0.48	5.12	−836.28	−881.77	−0.92	−1.86
Mn_2IrIn	it	−0.15	0.01	0.05	[−3.32, 3.38, −0.02, 0.01]	888	0.64	4.95	−686.49	−717.11	0.11	0.94
Mn_2NiGe	it	−0.22	0.00	0.37	[−2.46, 2.75, 0.06, 0.00]	917	0.32	5.02	−14.88	−97.78	−0.14	−0.69
Mn_2NiSn	it	−0.08	0.07	0.38	[−3.00, 3.31, 0.04, 0.01]	761	0.40	6.08	167.06	273.11	0.38	0.81
Mn_2OsGe	it	−0.13	0.00	0.03	[2.74, −2.85, 0.16, −0.01]	706	0.89	3.54	194.50	497.76	0.92	−1.77
Mn_2PdIn	it	−0.15	0.11	0.28	[−3.46, 3.67, 0.04, 0.01]	346	0.21	5.84	33.27	177.18	−0.01	1.53
Mn_2PdSn	it	−0.19	0.10	0.24	[−3.37, 3.57, 0.02, 0.01]	743	0.13	4.80	22.92	−141.62	0.18	−0.52
Mn_2PtSn	it	−0.23	0.09	0.04	[3.48, −3.43, 0.00, 0.00]	724	0.11	4.16	153.43	250.79	0.27	1.28
Mn_2ReGe	it	−0.07	0.05	0.22	[2.48, −2.53, 0.27, −0.01]	681	0.31	5.66	−564.75	−626.18	1.56	−1.76
Mn_2RhAl	it	−0.48	0.07	0.23	[−2.90, 3.11, 0.01, 0.00]	1066	0.50	5.64	−510.42	−658.36	−0.13	1.54
Mn_2RhGa	it	−0.40	0.00	0.16	[−3.06, 3.21, 0.00, 0.01]	1102	0.56	5.52	−221.33	−548.43	0.33	1.12
Mn_2RhIn	it	−0.19	0.03	0.01	[−3.46, 3.46, 0.00, 0.01]	996	0.73	4.81	71.17	518.14	−0.60	−1.99
Mn_2RuGa	it	−0.25	0.00	0.23	[3.02, −3.01, 0.23, −0.02]	1170	0.00	4.69	−191.07	377.05	−1.17	−1.59
Mn_2RuIn	it	−0.00	0.05	0.14	[3.32, −3.35, 0.18, −0.02]	1147	0.13	4.99	−97.71	−625.15	−1.08	−1.78
Mn_2RuSb	it	−0.07	0.03	0.20	[−2.94, 3.09, 0.01, 0.01]	568	0.41	6.35	−357.75	−692.35	−0.30	1.14
Mn_2RuSn	it	−0.11	0.00	0.02	[3.13, −3.22, 0.13, −0.01]	850	0.80	5.01	278.54	579.82	−1.72	2.02
Mn_2Si	hc	−0.19	0.18	0.01	[1.29, −1.33, 0.02]	1137	0.67	0.53	−0.04	−304.74	0.05	−0.95
MnCrAs	hc	−0.13	0.05	0.00	[−1.45, 1.45, −0.02]	1690	0.87	2.82	125.80	448.74	−0.16	−1.05
Ti_2CrSn	ic	−0.13	0.19	0.00	[1.33, 0.98, −2.64, 0.02]	1691	0.96	3.73	56.23	85.79	−0.09	0.33
V_2ScGa	ic	−0.05	0.25	0.30	[−1.43, 1.57, 0.15, 0.00]	585	0.47	9.21	−468.32	−468.32	−1.08	−1.98
V_2TiSn	ic	−0.08	0.14	0.04	[1.42, −0.67, −0.69, 0.00]	700	0.22	1.74	−25.56	88.31	0.07	−0.35

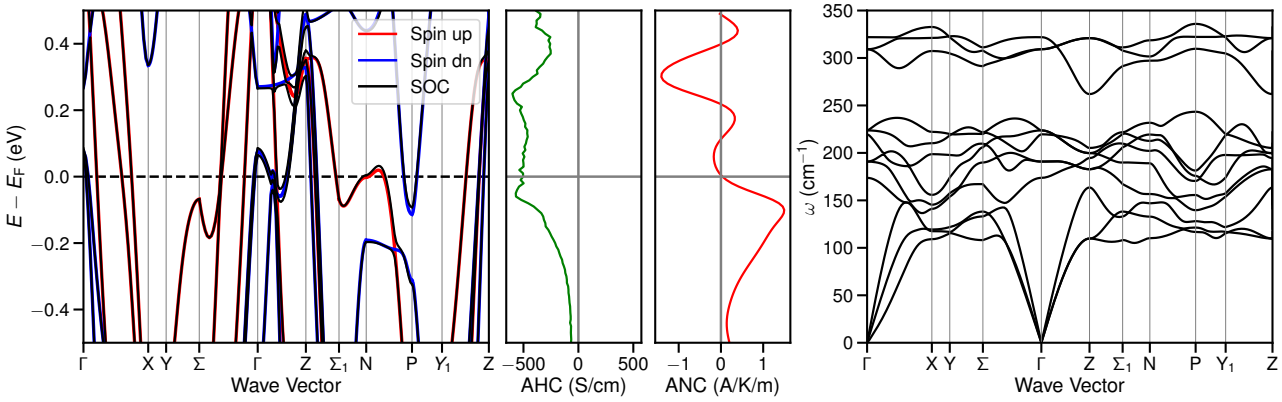

FIG. 2. Calculated electronic band structures with and without spin-orbit coupling, AHC, ANC, and the phonon band structure of inverse tetragonal Mn_2RhAl.

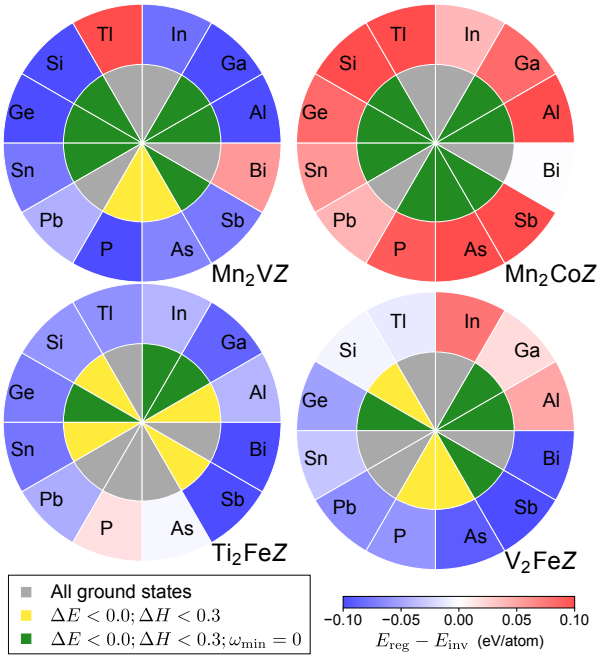

FIG. 3. Structural preference and stability of Mn_2VZ, Mn_2CoZ, Ti_2FeZ and V_2FeZ compounds. The pie chart slices are arranged by the Z element group. The inner circle indicates the stability categorized into three levels, while the outer-circle color map represents the energy difference $E_{\rm reg} - E_{\rm inv}$ in the range $[-0.1\,,\,0.1]$ eV/atom. Blue and red indicate preference for regular and inverse structures, respectively. Values outside this range are capped at the boundary values.

realization of the CFiM candidate would require careful optimization of the synthesis conditions.

Besides the discovery of promising candidates, the comprehensive HTP dataset also provides insights into the stability and structural preference in Heusler space. For example, X_2YZ has a preference for either the regular structure or the inverse structure over the other. For visualizing the distribution of regular and inverse structures and their relative stability, pie charts were used, as shown in Fig. 3, using Mn_2VZ, Mn_2CoZ, Ti_2FeZ, and V_2FeZ as examples. The pie chart slices are arranged by the Z element. The inner circle indicates stability, while the outer-circle color map represents the energy difference $E_{\rm reg} - E_{\rm inv}$. In the inner circle, the stability level is classified into three categories based on ΔE, ΔH, and $\omega_{\rm min}$. Here, $\omega_{\rm min}$ is the minimum value of the computed phonon frequencies on the commensurate $\boldsymbol{q}$ points and is shown as a negative value when it is imaginary. Hence, $\omega_{\rm min} = 0$ holds when the compound is dynamically stable. Given that the preference for regular or inverse structures is significant when the energy difference exceeds 0.1 eV/atom, the color map is capped at 0.1 eV/atom. In these examples, Mn_2VAl and Mn_2VGa are both stable and prefer the regular structure, while Mn_2CoAl, Mn_2CoGa, Mn_2CoGe, Mn_2CoSn, and Mn_2CoSb are stable and exhibit a preference for the inverse structure, consistent with experimental data [6]. The coexistence of regular and inverse structures has also been experimentally observed in compounds such as Ti_2FeAl, Ti_2FeGa, V_2FeAl, and V_2FeGa [20, 21]. The pie charts in Fig. 3 show the small energy differences ($E_{\rm reg} - E_{\rm inv}$) in these cases, which explain the coexistence of regular and inverse structures.

Using this visualization style, we generated a comprehensive stability and regular/inverse preference map for all X_2YZ compounds, shown in Fig. 4. The x- and y-axes correspond to the X and Y elements, respectively, while each pie chart represents the stability and structural preferences of 12 compounds with varying Z elements. This visualization style provides a clear and comprehensive overview of stability and structural preferences over X, Y, and Z compositions. Most stable inverse compounds are distributed in the lower left corner of the map, aligning with the empirical rule. However, a significant number of stable regular compounds are also located in this region. A detailed discussion of the regular/inverse preference is provided in subsection IV D.

We also generated maps for other competition pairs. For compounds with the same X, Y, and Z elements, the preference between X_2YZ and XYZ compositions is determined by the Hull distance difference between the half-Heusler and the lower energy regular or inverse Heusler compound. For a given composition and atomic arrangement, the competition between cubic and tetragonal phases is determined by the energy difference between the two phases. Comprehensive maps illustrating the competition between X_2YZ/XYZ compositions and cubic/tetragonal phases are provided in the Supplemental Material. These visualizations offer a clear and comprehensive overview to aid further study in Heusler compounds space.

IV. DISCUSSION

A. Magnetic critical temperature ($T_{\rm c}$)

The $T_{\rm c}$ values were computed within the mean-field approximation where the exchange coupling constants (J_{ij}) were obtained using the magnetic force theorem, as implemented in the SPRKKR code. The DFT calculations based on the KKR method were performed either within the ASA or using the FP method. To assess the reliability of the computed $T_{\rm c}$ values, we first compare the results with experimental data from previous high-throughput studies by Sanvito *et al.* [6] and Hu *et al.* [18], as shown in Fig. 5 (a). Overall, the calculated $T_{\rm c}$ values show good agreement with the experimental data. The $T_{\rm c}$ values obtained using the ASA exhibit considerable scatter, sometimes exceeding and sometimes falling below the experimental values. In contrast, the FP-base $T_{\rm c}$ values are consistently higher than the experimental data, which is reasonable given the mean-field approximation's tendency to overestimate $T_{\rm c}$ [68]. After applying a correction

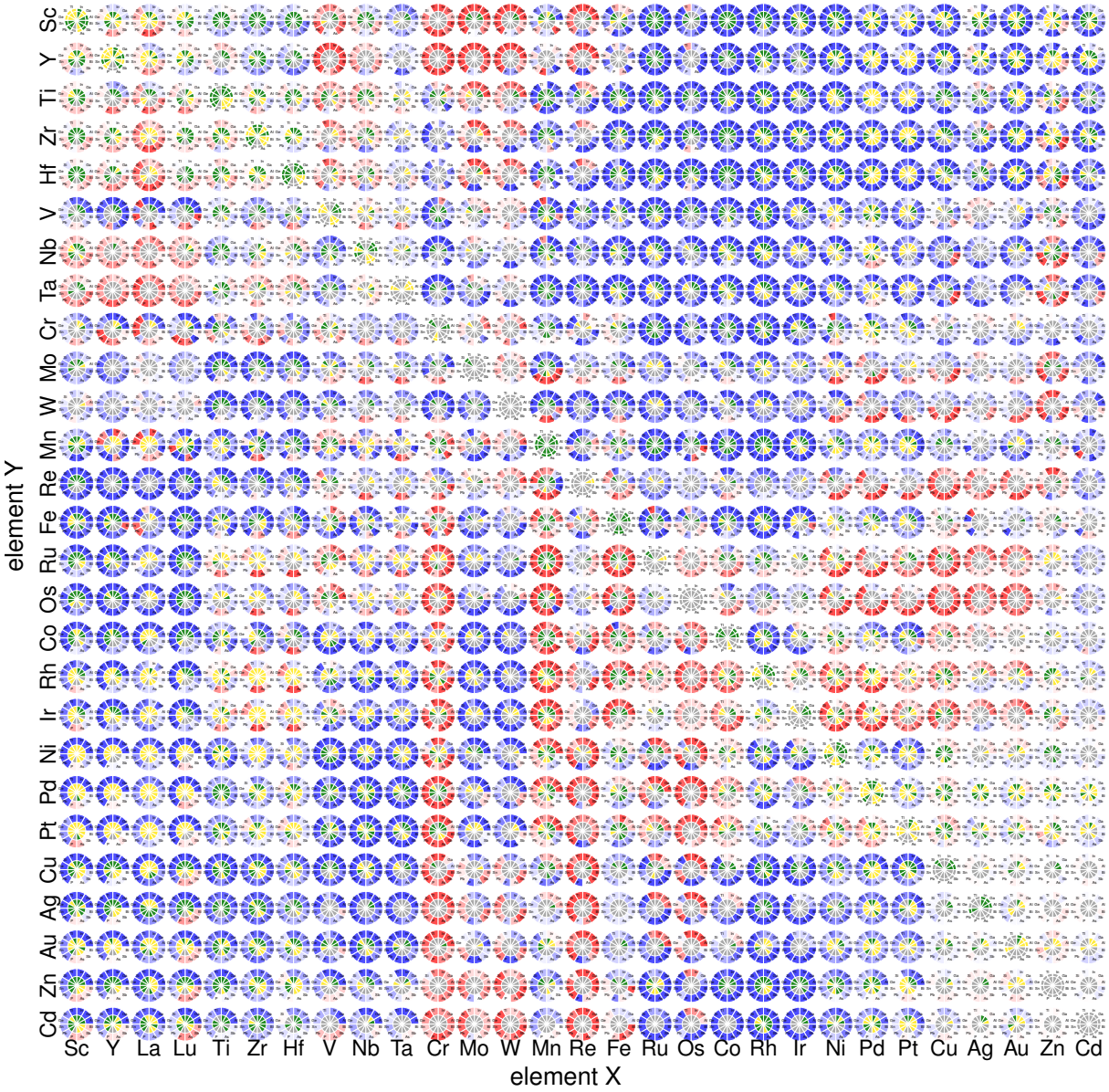

FIG. 4. Comprehensive stability and structural preference map for X_2YZ Heusler compounds. The x and y axes represent the X and Y elements, respectively. The order of elements is sorted by the group number for convenient comparison with empirical Burch's rule. Each pie chart corresponds to 12 compounds with the same X and Y elements but different Z elements arranged in the same style as Fig. 3. The inner circle indicates stability, while the outer circle represents $E_{\mathrm{reg}} - E_{\mathrm{inv}}$ in the range $[-0.1\,, 0.1]$ eV/atom. Blue/red indicates a preference for regular/inverse structures. Values outside this range are capped.

factor 0.85 to the FP-based T_{c} values, the results align well with the experimental data, achieving an R^2 score of 0.87. This adjustment compensates for the overestimation inherent in mean-field theory, and the result is satisfactory for high-throughput screening purposes.

Additionally, a consistency check of the calculation method was performed by comparing our calculated T_{c} values with those reported by Hu *et al.* in Ref. [18], which also utilized the SPRKKR code and shown as a black empty circle in Fig. 5. In Ref. [18], T_{c} values were primarily calculated using the ASA, whereas the FP-based computation was conducted only when the magnetization from the ASA results was inconsistent with the VASP magnetization. Consequently, some T_{c} values align with our ASA results, while others align with our FP-based calculations. Additionally, there are four cases—Co_2MnAl, Co_2MnGa, Mn_2CoGa, and Mn_2CoSn—where the results obtained by Hu *et al.* differ from both the ASA and FP values in our study. These discrepancies arise from differences in the identified ground states.

A previous study identified a linear relationship between the experimental T_{c} and total magnetization in Co_2-based ferromagnetic Heusler compounds across 10

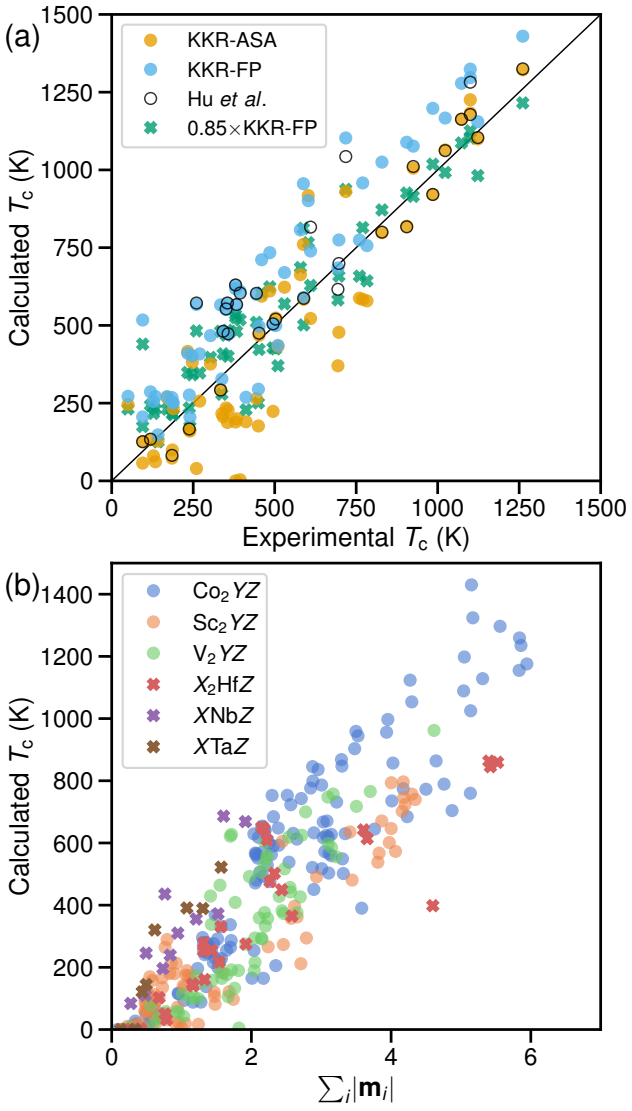

FIG. 5. (a) Comparison of calculated and experimental T_c. Calculated T_c values using ASA and FP methods are shown, along with FP results corrected by a factor of 0.85. Experimental data are from Refs. [6, 18]. (b) The distribution of calculated T_c via FP approach as a function of absolute sum of local magnetic moment $\sum_i |\boldsymbol{m}_i|$ in 6 Heusler compound systems.

different compositions [15]. Our calculated T_c values, obtained via the FP approach, exhibit the same trend in certain systems. Fig. 5 (b) illustrates the distribution of T_c values for six Heusler compound systems as a function of the absolute sum of local magnetic moments, $\sum_i |\boldsymbol{m}_i|$. The total magnetization is generalized to $\sum_i |\boldsymbol{m}_i|$ since there are FiM and AFM compounds in our HTP results. Besides Co_2YZ compounds, this linear relationship is also observed in other Heusler systems, including Sc_2YZ, V_2YZ, X_2HfZ, $XNbZ$, and $XTaZ$, as shown in Fig. 5(b). Notably, while the linear trend holds across these systems, the slope varies. For instance, the slope of $XNbZ$ compounds is significantly steeper than that of Sc_2YZ compounds. Overall, we identified five systems with an R^2 score exceeding 0.8 and nine additional systems with an R^2 score above 0.7. The corresponding linear fit coefficients and R^2 scores are listed in Table II. For systems with high R^2 values, this linear relationship can be used to estimate the T_c of new compounds. The distributions of T_c values versus $\sum_i |\boldsymbol{m}_i|$, categorized by X or Y element species, are provided in Fig. S3 and S4 in the Supplemental Material, along with the corresponding linear fit coefficients and R^2 scores.

TABLE II. Linear fit coefficients and R^2 scores for the correlation between T_c and the absolute sum of local magnetic moments, $\sum_i |\boldsymbol{m}_i|$. The linear relationship is expressed as $T_c = a\sum_i |\boldsymbol{m}_i| + b$. Results are presented for cases with data points number N larger than 10 and R^2 scores exceeding 0.7.

system	N	a	b	R^2	system	N	a	b	R^2
X_2CoZ	96	217	−145	0.77	Lu_2YZ	33	146	−84	0.85
Sc_2YZ	79	168	−36	0.87	Y_2YZ	31	116	−25	0.85
Ti_2YZ	64	363	−163	0.71	X_2HfZ	28	155	27	0.78
V_2YZ	64	241	−127	0.72	X_2NbZ	24	164	8	0.79
X_2TiZ	60	164	−41	0.73	Co_2YZ	132	220	−24	0.83
$CoYZ$	39	252	−69	0.77	Fe_2YZ	125	211	−141	0.73
X_2ScZ	37	124	38	0.72	$XNbZ$	12	363	−34	0.80

The distribution of ferrimagnet (FiM) compounds among the 1,356 magnetic materials is noteworthy. Specifically, 12 (1%) are antiferromagnetic, and 636 (47%) are FiM. All FiM compounds contain one or more of the following elements: Mn, Cr, Fe, V, Co, or Ti. The counts of FiM compounds containing Mn, Cr, Fe, V, Co, and Ti are 262, 123, 122, 120, 92, and 55, respectively. In comparison, the counts of ferromagnetic compounds containing these elements are 140, 41, 163, 47, 170, and 95, respectively. The ratio of FiM ordering is high in compounds containing Mn, Cr, and V. This is in agreement with a synthesis of such compounds in experiments [69–71]. Detailed distributions of magnetic ordering, categorized by element species and full/inverse/half Heusler structures, are presented in Fig. S5 of the Supplemental Material.

B. Refine stability criteria using experimental data

The stability of Heusler compounds was evaluated using three criteria: formation energy (ΔE), Hull distance (ΔH), and minimum phonon frequency ($\omega_{\min}$). The distribution of X_2YZ composition compounds across these metrics is shown in Fig. 6. For each X_2YZ composition, the structure (regular or inverse) with lower energy is selected. Formation energy values are evenly distributed, peaking around 0 eV/atom. For minimum phonon frequency, a sharp peak at $0\,\mathrm{cm}^{-1}$ reflects that approximately half of the thermodynamically stable compounds are also phonon-stable.

To assess the reliability of these stability criteria, we compare the stable compound dataset from first-

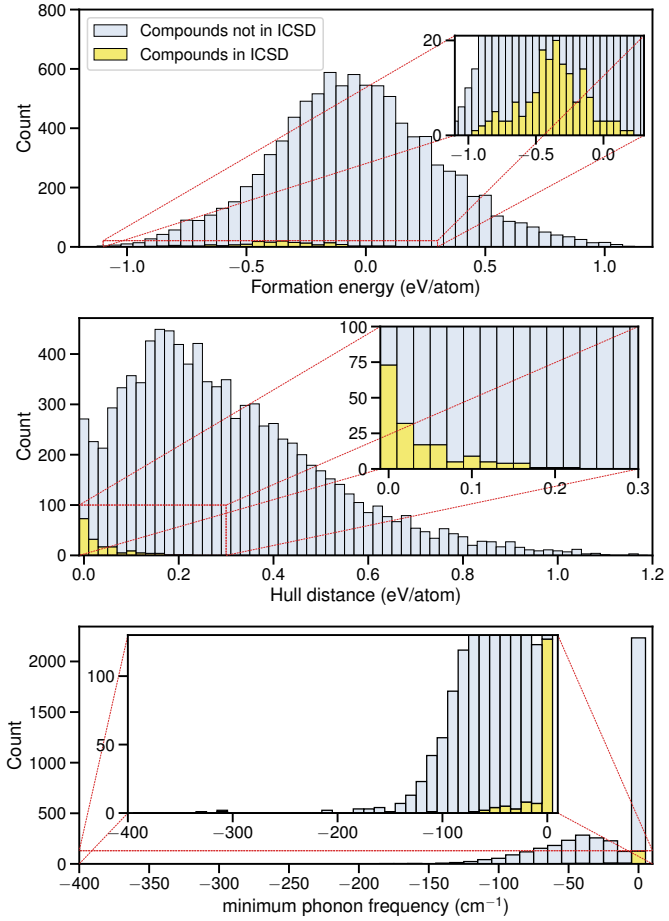

FIG. 6. Distribution of X_2YZ compounds ground states over formation energy, Hull distance, and minimum phonon frequency. Minimum phonon frequency distribution includes only compounds with $\Delta E < 0.0$ eV/atom and $\Delta H < 0.3$ eV/atom. The number of compounds included in ICSD database are shown as yellow bins.

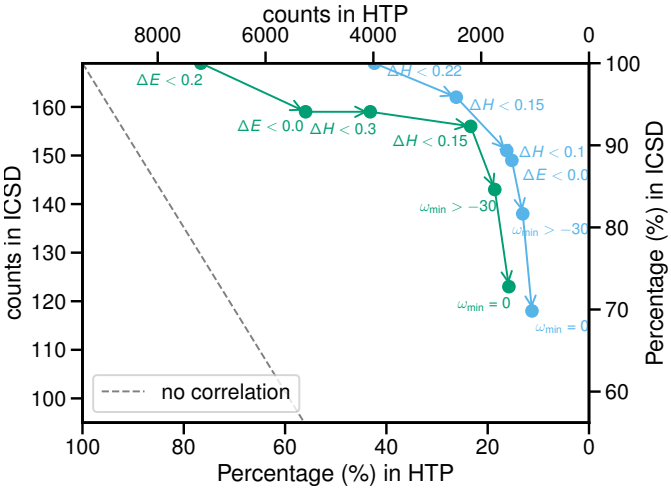

FIG. 7. Performance of *ab initio* stability criteria validated against ICSD experimental data. The x axis shows the counts and percentages of HTP compounds satisfying sequentially applied stability criteria, while the y axis indicates the counts and percentages of ICSD compounds included in the subset. If a criterion has no correlation with stability, it would fall on the diagonal line colored as gray.

principles predictions to experimentally synthesized compounds from the Inorganic Crystal Structure Database (ICSD) [72]. The ICSD contains 169 X_2YZ and 21 XYZ Heusler compounds. The distributions of ΔE, ΔH, and ω_{min} of the ICSD-registered X_2YZ compound are overlaid in Fig. 6. Additional figures for XYZ compounds are provided in the Supplemental Material.

Among the 169 X_2YZ compounds from the ICSD, 159 (94%) exhibit formation energies below 0 eV/atom, underscoring that negative formation energy is a robust necessary condition for stability prediction with large recall. A few ICSD compounds have positive calculated formation energies of up to 0.2 eV/atom. Since formation energy is calculated at 0 K, the observed stability of these compounds in experiments might be due to the stabilizing effect of entropic contributions at finite temperatures. Additionally, the positive values could be attributed to uncertainties in DFT calculations. In a compound search task prioritizing the identification of as many candidates as possible, a relaxed threshold of ΔE is a reasonable choice.

The hull distance values for most ICSD-registered Heuslers are close to zero. A few ICSD data extend up to $\Delta H = 0.22$ eV/atom, which is lower than the $\Delta H < 0.3$ eV/atom threshold used in the HTP workflow. Using a threshold of $\Delta H < 0.22$ eV/atom enhances precision without compromising recall of ICSD data, while a stricter threshold of $\Delta H < 0.10$ eV/atom can narrow down the candidate list by 62% compared to $\Delta H < 0.22$ eV/atom list, at the cost of a smaller recall (89%).

The distribution of ω_{min} for compounds with $\Delta E < 0$ eV/atom and $\Delta H < 0.3$ eV/atom is presented in Fig. 6, including 159 compounds from the ICSD. Imaginary phonon modes (represented as $\omega_{\text{min}} < 0$) indicate structural phase transitions and thus render the structures dynamically unstable, as observed in compounds such as Pd_2TiSn, Pd_2ZrSn, and Pd_2HfSn at low temperatures [73]. Among the ICSD compounds, 124 (78%) exhibit $\omega_{\text{min}} = 0$, affirming that the calculated phonon stability serves as a good criterion for stability. The remaining 35 ICSD compounds display ω_{min} values ranging from -0.5 to -71.4 cm^{-1} and two points at -111.0 cm^{-1} and -308.9 cm^{-1}. The number of compounds with negative ω_{min} values decreases as the magnitude of ω_{min} becomes larger.

These predictions are based on phonon dispersion within the harmonic approximation. It should be noted that this approach does not account for anharmonic effects, which can stabilize systems with imaginary phonon modes at finite temperatures [45, 73, 74]. The 35 ICSD compounds with negative ω_{min} values may become dynamically stable when anharmonic effects are included at finite temperatures. However, due to the complexity and high computational cost associated with treating anharmonic effects, a more practical strategy is to use ω_{min} computed at the harmonic level and choose a threshold value at a balance of precision and recall based on the specific application. For instance, a threshold of

$\omega_{\text{min}} = 0$ cm^{-1} is recommended for tasks prioritizing reliable candidates, whereas a threshold of $\omega_{\text{min}} > -70$ cm^{-1} is suitable for identifying a broader range of potential candidates.

As shown in Fig. 6, applying stricter criteria increases the precision of stability predictions, as the ratio of removed compounds is larger in the HTP than the ICSD data, while recall is reduced. Figure 7 illustrates the number of the HTP compounds that meet various stability criteria applied sequentially and the number of the ICSD-registered Heuslers included within this subset. The x-axis represents the numbers/percentages of HTP compounds that satisfy various stability criteria applied sequentially. The number decreases as the criteria become stricter. The y-axis represents the numbers/percentages of ICSD compounds included in each set of HTP compounds. The location of the points in the plot indicates the trade-off between precision and recall. If a criterion has no correlation with stability, it would fall on the gray diagonal line. By switching the order in which ΔE and ΔH are applied, it is clear that ΔH is a more effective criterion for identifying thermodynamically stable compounds.

When using the criteria $\Delta E < 0.0$ eV/atom and $\Delta H < 0.3$ eV/atom, 4,058 (43%) of HTP compounds are predicted to be stable, and 159 (94%) ICSD compounds are correctly identified as stable. When $\omega_{\text{min}} = 0$ cm^{-1} is added as a criterion, 2,173 (23%) of HTP compounds are predicted to be stable, and 124 (78%) ICSD compounds are correctly identified as stable. This demonstrates the validity of the stability criterion choice in our workflow.

From Fig. 7, we can identify optimal criteria for different HTP screening task types quantitatively. In a screening task prioritizing the identification of as many stable compounds as possible, a relaxed threshold of ΔE is a reasonable choice. Using criteria $\Delta E < 0.2$ eV/atom and $\Delta H < 0.22$ eV/atom, 3,968 (42%) of HTP compounds are predicted to be stable, and all ICSD compounds are correctly identified as stable. This set of criteria offers the best recall. Conversely, with the criteria $\Delta E < 0.0$ eV/atom, $\Delta H < 0.10$ eV/atom, and $\omega_{\text{min}} = 0$ cm^{-1}, 1,057 (10%) HTP compounds are predicted to be stable, and 118 (70%) ICSD compounds are correctly identified as stable. This set of criteria is expected to provide good precision, albeit with a trade-off in recall.

Similar trends are observed for half-Heusler compounds, where 1181 (13%) HTP compounds meet the criteria of $\Delta E < 0.0$ eV/atom and $\Delta H < 0.3$ eV/atom. Of 21 half-type ICSD compounds, 19 meet the same criteria. The exception CuMnSb has small $\Delta E = 0.05$ eV/atom and $\Delta H = 0.07$ eV/atom. While the other exception CoCrAl has large $\Delta H = 0.44$ eV/atom, the reported experimental structure of CoCrAl has Cr occupying 50% $(\frac{1}{2}, \frac{1}{2}, \frac{1}{2})$ and 50% $(\frac{3}{4}, \frac{3}{4}, \frac{3}{4})$ Wyckoff positions, which is not standard half Heusler structure used in our computation [75]. The stability observed in experiments may be due to the disorder. When $\omega_{\text{min}} = 0$ cm^{-1} is added as a criterion, 842 (9%) HTP compounds are predicted to be stable, and 18 (85%) ICSD compounds are correctly identified as stable.

C. Stability and atomic feature

From the HTP calculation results, a correlation between stability and atomic properties is identified. For X_2YZ compounds, stability is favored when the Z element has a small atomic radius and low ionization energy. Figure 8 shows the distribution of X_2YZ type compounds over Z element species, along with the Z element's first ionization energy (I_1) and atomic radius (r_{atom}) [76–78]. Each bin represents the counts of compounds that contain the corresponding Z element. The compounds are divided into different stability groups indicated by various colors. The local and global trends in stable compound distribution are consistent with the trends in I_1 and r_{atom}, respectively. For comparison, the distribution of half-Heusler compounds is also shown, where no such correlation is found. Among the phonon-stable X_2YZ compounds, 51% contain either Al, Ga, or In as the Z element, and 26% contain either Si, Ge, or Sn. These elements should be prioritized for discovering stable functional Heuslers. This observation is expected to be valid for more general Heusler compounds, such as quaternary and off-stoichiometric types.

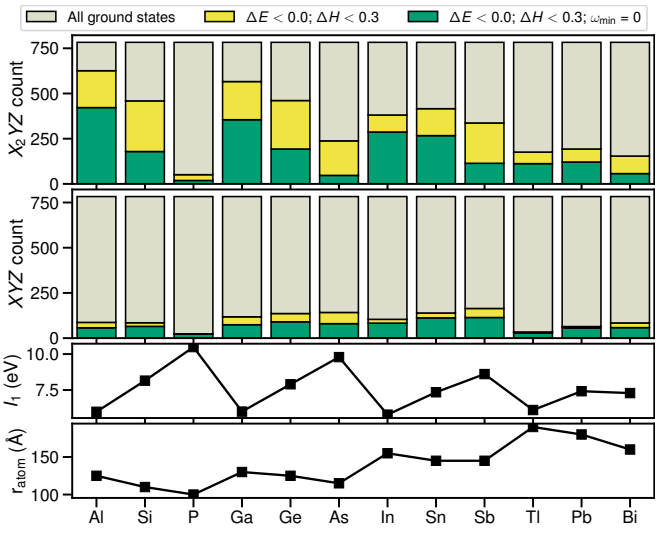

FIG. 8. Distributions of X_2YZ and half-type compounds over Z element species, with different stability groups shown in various colors. First ionization energy (I_1) and atomic radius (r_{atom}) of Z elements are sourced from [76–78].

In half-Heusler compounds, stability is higher when the X element has a smaller atomic radius compared to the Y element. Figure 9 shows the distribution of half-Heusler compounds over X and Y element species, along with the atomic radii of the X and Y elements. It is evident that stable compounds are concentrated in the region where the X element has a smaller atomic radius, and

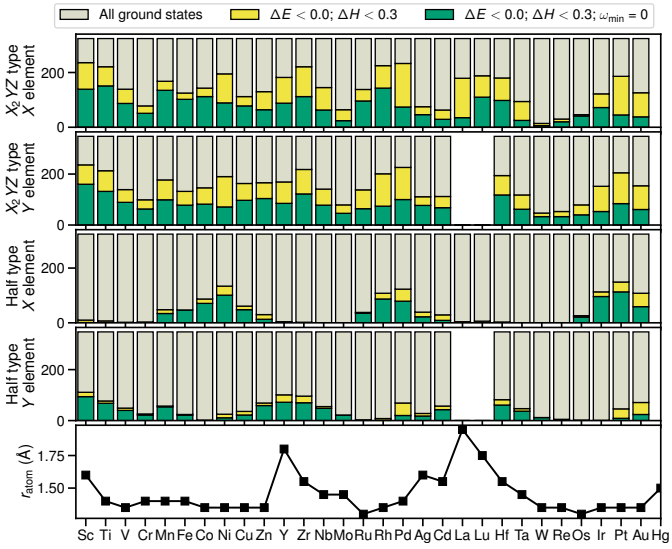

FIG. 9. Distributions of X_2YZ and half-type compounds over X or Y element species, with different stability groups shown in various colors. Atomic radius (r_{atom}) of X and Y elements are sourced from [76, 77].

the Y element has a larger radius. For comparison, the distribution of X_2YZ compounds is also shown in Figure 9, where no such correlation is observed. Notably, 94% of stable half-Heusler compounds satisfy the condition $r^X_{\text{atom}} \leq r^Y_{\text{atom}}$. This provides a robust necessary condition for selecting stable half-Heusler candidates.

D. Regular or inverse structure preference in X_2YZ compound

Understanding the preference for regular or inverse structures in X_2YZ compounds is crucial for tailoring their functional properties. Figure 10(a) shows the distribution of X_2YZ compounds based on the energy difference between regular and inverse structures ($E_{\text{reg}} - E_{\text{inv}}$). Overall, the regular structure is generally preferred across all X_2YZ compounds analyzed. This trend remained consistent when various stability criteria were applied.

The structural preference analysis for regular or inverse configurations in X_2YZ compounds is often guided by Burch's rule [18–22] According to this empirical rule, if the Y element is positioned to the left of the X element in the periodic table, the compound is more likely to adopt a regular structure. Conversely, if the Y element is to the right of the X element, an inverse structure is favored. This trend can be quantitatively represented using electronegativity differences ($\chi^X - \chi^Y$), as electronegativity generally increases from left to right across the periodic table [18]. A negative value of $\chi^X - \chi^Y$ indicates that Y is to the right of X, favoring an inverse structure.

This relationship is examined using our HTP calculation results and illustrated in Fig. 10(b). The preference is shown by color-coded energy difference ($E_{\text{reg}} - E_{\text{inv}}$), along with the electronegativity difference ($\chi^X - \chi^Y$) and covalent radius difference ($r^X_{\text{cov}} - r^Y_{\text{cov}}$) between X and Y elements are shown on the x- and y-axes, respectively. The results are shown for all compounds (5,388) and for the subsets (1,294) meeting the stability criteria. Inverse structures tend to occur when $\chi^X - \chi^Y < 0$, in accordance with Burch's rule. This pattern remains even after considering the stability criteria.

Additionally, when stability criteria are applied, stable inverse structures generally have X and Y elements with similar covalent radii. This observation aligns with the expectation that X and Y elements should be similar in size in inverse structures, as their positions are interchanged compared to regular structures. The region defined by $\chi^X - \chi^Y < 0.15$ eV and $|r^X_{\text{cov}} - r^Y_{\text{cov}}| < 0.20$ Å is highlighted in green, marking a range where structural preferences are distinct. Among the 490 stable inverse compounds identified, 390 (80%) fall within this region. However, the number of regular compounds satisfying these criteria is comparable to inverse compounds, indicating that these criteria are robust necessary conditions but not sufficient. Conversely, for regular structure prediction, the criteria exhibit high precision (92%) but lower recall (75%).

E. Tetragonal distortion

Heusler compounds typically crystallize in either the cubic or tetragonal phase. Our HTP computational study revealed that 7,959 X_2YZ-type and 6,909 half-Heusler compounds exhibit tetragonal distortion in their ground state. The primary factor contributing to tetragonal distortion is commonly thought to be the peaks in the density of states (DOS) near the Fermi level (E_F) in the cubic phase DOS(cubic, E_F) [79]. This conclusion was supported by the previous high-throughput studies on several hundred X_2YZ compounds containing Fe, Co, and Ni [23, 79–81]. The same conclusion is drawn from our HTP result spanning significantly broader elemental space. The distribution of X_2YZ type compounds up to DOS(cubic, E_F)=15 eV^{-1} is shown in Fig.11. The counts of cubic and tetragonal Heusler compounds are sorted into bins based on their DOS(cubic,E_F) values. The red curve represents the probability of tetragonal distortion in each bin. The probability of distortion increases as DOS(cubic, E_F) rises. When DOS(cubic, E_F) exceeds 3 eV^{-1}, the probability of tetragonal distortion is greater than 80%. The same analysis was extended to Half-Heusler compounds, and a similar behavior was found. When DOS(cubic, E_F) exceeds 3 eV^{-1}, the probability of tetragonal distortion is greater than 70%.

It is worth noting that the inclusion of stability criteria alters the distributions, as shown in the middle and right panels of Fig. 11. For half-Heusler compounds, tetragonal distortion is observed in 74% of all compounds, but this drops to 31% when only phonon-stable compounds are considered. The low ratio in stable com-

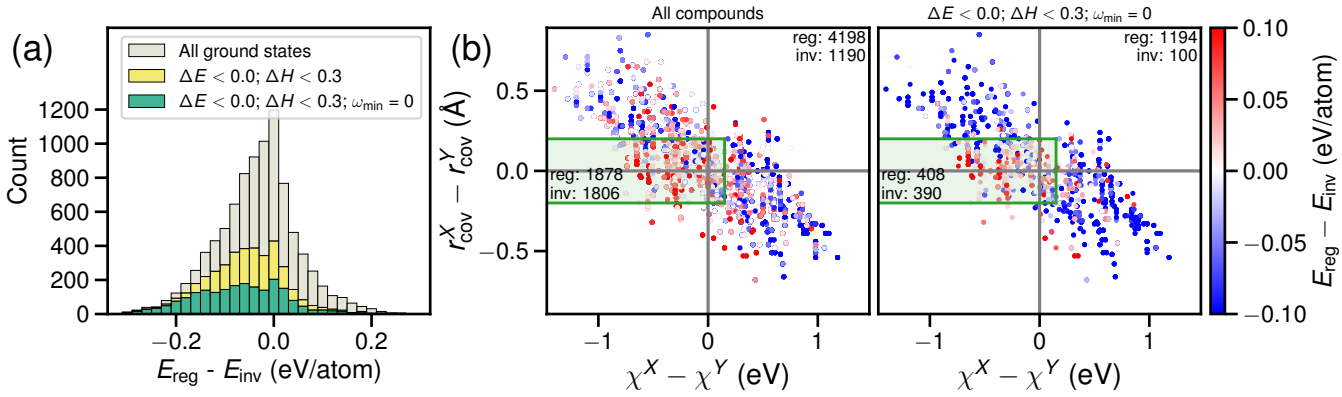

FIG. 10. (a) Distribution of X_2YZ compounds based on the energy difference between regular and inverse structures ($E_{\rm reg} - E_{\rm inv}$). Different stability groups are represented by various colors. (b) Regular/inverse preference of compounds meeting various stability criteria. The preference is shown by the energy difference ($E_{\rm reg} - E_{\rm inv}$), which is color-coded. The electronegativity difference ($\chi^X - \chi^Y$) and covalent radius difference ($r^X_{\rm cov} - r^Y_{\rm cov}$) between X and Y elements are shown on the x- and y-axes, respectively. The region where $\chi^X - \chi^Y < 0.15$ eV and $|r^X_{\rm cov} - r^Y_{\rm cov}| < 0.20$ Å is marked by green shading.

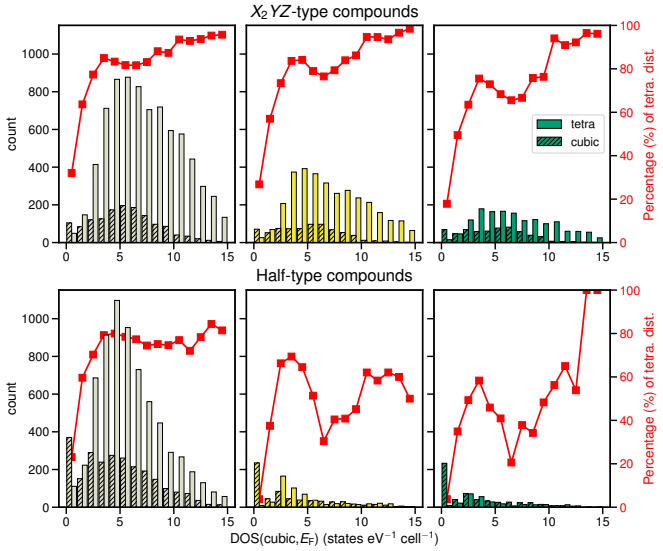

FIG. 11. Distribution of cubic and tetragonal Heusler compounds sorted into bins based on the density of states (DOS) values at the Fermi level in the cubic phase. The red curve represents the percentage of tetragonal distortion for each bin. The distributions are shown for all compounds (left panels), compounds meeting thermodynamic stability criteria (middle panels), and compounds additionally satisfying the dynamical stability criterion (right panels).

pounds indicates that half-Heusler compounds are less suitable for applications requiring tetragonal distortion, such as materials with high MCA. Similarly, the occurrence of tetragonal distortion in X_2YZ compounds decreases from 85% in all compounds to 72% among phonon-stable compounds.

V. CONCLUSION

In this study, we conducted a comprehensive high-throughput stability analysis of 9,072/9,072/324/9,396 compositions of regular/inverse/X_3Z/half-Heusler compounds in both cubic and tetragonal phases, considering various magnetic configurations. In total, 106,235 structures in ground states and metastable states were identified. By applying stability criteria to ground states based on formation energy, Hull distance, and phonon stability, we identified 1,898 regular, 1,192 inverse, 81 X_3Z, and 840 half-Heusler stable compounds. Among these, 1,356 compounds are magnetic, and 631 compounds exhibit $T_{\rm c}$ above 300 K, making them promising candidates for further experimental and theoretical exploration of new functional materials. Notably, we identified 47 low-moment FiM systems. The spin polarization and anomalous Hall/Nernst conductivity were calculated to evaluate their potential applications in spintronics and energy harvesting.

We validated the $T_{\rm c}$ calculation method within the mean-field approximation against experimental data and found that a simple correction factor of 0.85 to the Full-potential (FP)-based $T_{\rm c}$ provides a good agreement with experimental results. Also, we validated *ab initio* calculation stability criteria alongside experimental data from the ICSD, suggesting optimized criteria for achieving higher recall or accuracy, depending on application needs. Our results demonstrated that the inclusion of phonon stability significantly narrows the pool of viable candidates, emphasizing its critical role. We expect these $T_{\rm c}$ calibration methods and refined stability criteria to be valid to other types of Heusler compounds, such as all-d and quaternary types, as well as similar magnetic systems.

Analysis of the HTP data revealed linear relationships between $T_{\rm c}$ and $\sum_i |\boldsymbol{m}_i|$ in 14 Heusler compound

systems, which can be used to do rough estimation of T_c. We also identified correlations between stability and atomic properties, such as atomic radius and ionization energy. For regular/inverse preference in X_2YZ compounds, our findings aligned with the empirical Burch's rule and further indicated that inverse structures are more likely when the X and Y elements have similar covalent radii, although this condition is not sufficient to guarantee an inverse structure formation. In terms of tetragonal distortion, we confirmed a strong correlation between tetragonal distortion and a high density of states at the Fermi level in the cubic phase in X_2YZ compounds, in agreement with the previous work, and identified a similar correlation in half-Heusler compounds.

Overall, these insights extend our understanding of stability and structural preferences in Heusler compounds, providing a foundation for more efficient material discovery in this and related categories. By refining the criteria for stability and identifying key atomic correlations, this work contributes to the development of next-generation functional materials. The comprehensive dataset produced in this work, comprising 106,235 entries of the crystal structures, magnetic moments, and the corresponding energies, 8,180 entries of phonons, 1,356 entries of T_c, and 355 entries of AHC/ANC, is available at [82]. This database will be useful not only for querying the stability of Heuslers but also for developing machine-learning models. Development and application of such a machine learning model based on our database, aiming to explore more complicated functional Heuslers efficiently, are ongoing and will be present elsewhere.

DECLARATION OF COMPETING INTEREST

The authors declare that they have no known competing financial interests or personal relationships that could have appeared to influence the work reported in this paper.

ACKNOWLEDGMENTS

This study was supported by MEXT Program: Data Creation and Utilization-Type Material Research and Development Project (Digital Transformation Initiative Center for Magnetic Materials) Grant Number JPMXP112271550 and as "Program for Promoting Researches on the Supercomputer Fugaku" (Data-Driven Research Methods Development and Materials Innovation Led by Computational Materials Science, JPMXP1020230327). This study used computational resources of supercomputer Fugaku provided by the RIKEN Center for Computational Science (Project ID: hp240223), the computer resources provided by ISSP, U-Tokyo under the program of SCCMS, and the computer resources at NIMS Numerical Materials Simulator.

[1] H. Zhang, Electron. Struct. **3**, 033001 (2021).
[2] M. Gilleßen and R. Dronskowski, J. Comput. Chem. **30**, 1290 (2009).
[3] M. Gilleßen and R. Dronskowski, J. Comput. Chem. **31**, 612 (2010).
[4] J. Carrete, Phys. Rev. X **4**, 10.1103/PhysRevX.4.011019 (2014).
[5] S. V. Faleev, Y. Ferrante, J. Jeong, M. G. Samant, B. Jones, and S. S. P. Parkin, Phys. Rev. Mater. **1**, 024402 (2017).
[6] S. Sanvito, C. Oses, J. Xue, A. Tiwari, M. Zic, T. Archer, P. Tozman, M. Venkatesan, M. Coey, and S. Curtarolo, Sci. Adv. **3**, e1602241 (2017).
[7] Q. Gao, I. Opahle, and H. Zhang, Phys. Rev. Mater. **3**, 024410 (2019).
[8] M. Marathe and H. C. Herper, Phys. Rev. B **107**, 174402 (2023).
[9] J. Noky, Y. Zhang, J. Gooth, C. Felser, and Y. Sun, npj Comput. Mater. **6**, 1 (2020).
[10] M. Marathe and H. C. Herper, Phys. Rev. B **107**, 174402 (2023), publisher: American Physical Society.
[11] G. Xing, K. Masuda, T. Tadano, and Y. Miura, Acta Mater. **270**, 119856 (2024).
[12] S. Kirklin, J. E. Saal, B. Meredig, A. Thompson, J. W. Doak, M. Aykol, S. Rühl, and C. Wolverton, npj Comput. Mater. **1**, 1 (2015).
[13] M. Esters, C. Oses, S. Divilov, H. Eckert, R. Friedrich, D. Hicks, M. J. Mehl, F. Rose, A. Smolyanyuk, A. Calzolari, X. Campilongo, C. Toher, and S. Curtarolo, Comput. Mater. Sci. **216**, 111808 (2023).
[14] Enamullah and S.-C. Lee, J. Alloys Compd. **765**, 1055 (2018).
[15] S. Wurmehl, G. H. Fecher, H. C. Kandpal, V. Ksenofontov, C. Felser, H.-J. Lin, and J. Morais, Phys. Rev. B **72**, 184434 (2005).
[16] X.-Q. Chen, R. Podloucky, and P. Rogl, J. Appl. Phys. **100**, 113901 (2006).
[17] J. Balluff, Phys. Rev. Mater. **1**, 10.1103/PhysRevMaterials.1.034404 (2017).
[18] K. Hu, R. Xie, C. Shen, H. Peng, H. Liu, and H. Zhang, Acta Mater. **259**, 119255 (2023).
[19] T. J. Burch, T. Litrenta, and J. I. Budnick, Phys. Rev. Lett. **33**, 421 (1974).
[20] J. Goraus, M. Fijałkowski, J. Czerniewski, and W. Gumulak, J. Magn. Magn. Mater. **585**, 171103 (2023).
[21] J. Goraus and J. Czerniewski, J. Magn. Magn. Mater. **498**, 166106 (2020).
[22] G. Kreiner, A. Kalache, S. Hausdorf, V. Alijani, J.-F. Qian, G. Shan, U. Burkhardt, S. Ouardi, and C. Felser, Z. Anorg. Allg. Chem. **640**, 738 (2014).
[23] J. Winterlik, S. Chadov, A. Gupta, V. Alijani, T. Gasi, K. Filsinger, B. Balke, G. H. Fecher, C. A. Jenkins, F. Casper, J. Kübler, G.-D. Liu, L. Gao, S. S. P. Parkin,

and C. Felser, Adv. Mater. **24**, 6283 (2012).
[24] J. Finley and L. Liu, Appl. Phys. Lett. **116**, 110501 (2020).
[25] H. Kurt, K. Rode, P. Stamenov, M. Venkatesan, Y.-C. Lau, E. Fonda, and J. M. D. Coey, Phys. Rev. Lett. **112**, 027201 (2014).
[26] N. Thiyagarajah, Y.-C. Lau, D. Betto, K. Borisov, J. M. D. Coey, P. Stamenov, and K. Rode, Appl. Phys. Lett. **106**, 122402 (2015).
[27] D. Betto, N. Thiyagarajah, Y.-C. Lau, C. Piamonteze, M.-A. Arrio, P. Stamenov, J. M. D. Coey, and K. Rode, Phys. Rev. B **91**, 094410 (2015).
[28] A. K. Nayak, M. Nicklas, S. Chadov, P. Khuntia, C. Shekhar, A. Kalache, M. Baenitz, Y. Skourski, V. K. Guduru, A. Puri, U. Zeitler, J. M. D. Coey, and C. Felser, Nat. Mater. **14**, 679 (2015).
[29] R. Sahoo, L. Wollmann, S. Selle, T. Höche, B. Ernst, A. Kalache, C. Shekhar, N. Kumar, S. Chadov, C. Felser, S. S. P. Parkin, and A. K. Nayak, Adv. Mater. **28**, 8499 (2016).
[30] R. Stinshoff, Phys. Rev. B **95**, 10.1103/PhysRevB.95.060410 (2017).
[31] R. Gavrea, R. Hirian, O. Isnard, V. Pop, and D. Benea, Solid State Commun. **309**, 113812 (2020).
[32] S. Chatterjee, P. Dutta, P. Singha, S. Giri, A. Banerjee, and S. Majumdar, J. Magn. Magn. Mater. **532**, 167956 (2021).
[33] M. A. Seredina, D. Yu. Karpenkov, E. A. Kolesnikov, M. V. Gorshenkov, A. Yu. Degtyarenko, S. V. Taskaev, P. N. Degtyarenko, X. Xu, and V. V. Khovaylo, J. Magn. Magn. Mater. **562**, 169808 (2022).
[34] R. Harikrishnan, J. K. Bidika, B. R. K. Nanda, A. J. Chelvane, S. D. Kaushik, P. D. Babu, and H. K. Narayanan, Phys. Rev. B **108**, 094407 (2023).
[35] S. Wurmehl, H. C. Kandpal, G. H. Fecher, and C. Felser, J. Phys.: Condens. Matter **18**, 6171 (2006).
[36] D. Benea, R. Gavrea, M. Coldea, O. Isnard, and V. Pop, J. Magn. Magn. Mater. **475**, 229 (2019).
[37] Y. J. Zhang, Z. H. Liu, Z. G. Wu, and X. Q. Ma, IUCrJ **6**, 610 (2019).
[38] W. Shi, Phys. Rev. B **97**, 10.1103/PhysRevB.97.060406 (2018).
[39] J. Noky, Phys. Rev. B **97**, 10.1103/PhysRevB.97.220405 (2018).
[40] G. Kresse and J. Furthmüller, Comput. Mater. Sci. **6**, 15 (1996).
[41] G. Kresse and D. Joubert, Phys. Rev. B **59**, 1758 (1999).
[42] J. P. Perdew, K. Burke, and M. Ernzerhof, Phys. Rev. Lett. **77**, 3865 (1996).
[43] J. Ma, J. He, D. Mazumdar, K. Munira, S. Keshavarz, T. Lovorn, C. Wolverton, A. W. Ghosh, and W. H. Butler, Phys. Rev. B **98**, 094410 (2018), publisher: American Physical Society.
[44] W. Sun, S. T. Dacek, S. P. Ong, G. Hautier, A. Jain, W. D. Richards, A. C. Gamst, K. A. Persson, and G. Ceder, Sci. Adv. **2**, e1600225 (2016).
[45] T. Tadano and S. Tsuneyuki, Phys. Rev. B **92**, 054301 (2015).
[46] T. Tadano, Y. Gohda, and S. Tsuneyuki, J. Phys.: Condens. Matter **26**, 225402 (2014).
[47] H. Ebert, D. Ködderitzsch, and J. Minár, Rep. Prog. Phys. **74**, 096501 (2011).
[48] A. A. Mostofi, J. R. Yates, Y.-S. Lee, I. Souza, D. Vanderbilt, and N. Marzari, Comput. Phys. Commun. **178**, 685 (2008).
[49] N. Nagaosa, J. Sinova, S. Onoda, A. H. MacDonald, and N. P. Ong, Reviews of Modern Physics **82**, 1539 (2010).
[50] G. Kresse and J. Furthmüller, Phys. Rev. B **54**, 11169 (1996).
[51] M. Methfessel and A. T. Paxton, Phys. Rev. B **40**, 3616 (1989).
[52] P. E. Blöchl, Phys. Rev. B **49**, 16223 (1994).
[53] A. Jain, G. Hautier, C. J. Moore, S. Ping Ong, C. C. Fischer, T. Mueller, K. A. Persson, and G. Ceder, Comput. Mater. Sci. **50**, 2295 (2011).
[54] S. P. Ong, W. D. Richards, A. Jain, G. Hautier, M. Kocher, S. Cholia, D. Gunter, V. L. Chevrier, K. A. Persson, and G. Ceder, Comput. Mater. Sci. **68**, 314 (2013).
[55] A. H. Larsen, J. J. Mortensen, J. Blomqvist, I. E. Castelli, R. Christensen, M. Dułak, J. Friis, M. N. Groves, B. Hammer, C. Hargus, E. D. Hermes, P. C. Jennings, P. B. Jensen, J. Kermode, J. R. Kitchin, E. L. Kolsbjerg, J. Kubal, K. Kaasbjerg, S. Lysgaard, J. B. Maronsson, T. Maxson, T. Olsen, L. Pastewka, A. Peterson, C. Rostgaard, J. Schiøtz, O. Schütt, M. Strange, K. S. Thygesen, T. Vegge, L. Vilhelmsen, M. Walter, Z. Zeng, and K. W. Jacobsen, J. Phys.: Condens. Matter **29**, 273002 (2017).
[56] A. Togo, K. Shinohara, and I. Tanaka, Sci. Technol. Adv. Mater.: Methods **4**, 10.1080/27660400.2024.2384822 (2024).
[57] P. W. Anderson, in *Solid State Physics*, Vol. 14, edited by F. Seitz and D. Turnbull (Academic Press, 1963) pp. 99–214.
[58] A. I. Liechtenstein, M. I. Katsnelson, V. P. Antropov, and V. A. Gubanov, J. Magn. Magn. Mater. **67**, 65 (1987).
[59] T. Huhne, C. Zecha, H. Ebert, P. H. Dederichs, and R. Zeller, Phys. Rev. B **58**, 10236 (1998).
[60] ASE2SPRKKR (2022–).
[61] S. R. Bahn and K. W. Jacobsen, Comput. Sci. Eng. **4**, 56 (2002).
[62] A. Damle and L. Lin, Multiscale Model. Simul. **16**, 1392 (2018).
[63] A. Damle, L. Lin, and L. Ying, J. Chem. Theory Comput. **11**, 1463 (2015).
[64] D. Xiao, Y. Yao, Z. Fang, and Q. Niu, Phys. Rev. Lett. **97**, 026603 (2006).
[65] D. Xiao, M.-C. Chang, and Q. Niu, Rev. Mod. Phys. **82**, 1959 (2010), arXiv:0907.2021 [cond-mat].
[66] M. Julliere, Phys. Lett. A **54**, 225 (1975).
[67] Z. Ren, Y. Liu, S. Li, X. Zhang, and H. Liu, Mater. Sci.-Pol. **34**, 251 (2016).
[68] D. A. Garanin, Phys. Rev. B **53**, 11593 (1996).
[69] H. Itoh, T. Nakamichi, Y. Yamaguchi, and N. Kazama, Trans. Jpn. Inst. Met. **24**, 265 (1983).
[70] Z. Chen, W. Liu, P. Chen, X. Ruan, J. Sun, R. Liu, C. Gao, J. Du, B. Liu, H. Meng, R. Zhang, and Y. Xu, Appl. Phys. Lett. **117**, 012401 (2020).
[71] M. E. Jamer, G. E. Sterbinsky, G. M. Stephen, M. C. DeCapua, G. Player, and D. Heiman, Appl. Phys. Lett. **109**, 182402 (2016).
[72] A. Belsky, M. Hellenbrandt, V. L. Karen, and P. Luksch, Acta Crystallogr. Sect. B: Struct. Sci. **58**, 364 (2002).
[73] H. Su, F. Du, R. Li, S. Luo, Y. Chen, J. Liu, Y. Chen, C. Cao, M. Smidman, and H. Yuan, Phys. Rev. B **106**, 134517 (2022).

[74] T. Tadano and S. Tsuneyuki, Phys. Rev. Lett. **120**, 105901 (2018).
[75] A. Datta and I. Das, J. Magn. Magn. Mater. **563**, 169907 (2022).
[76] Ł. Mentel, mendeleev – a python resource for properties of chemical elements, ions and isotopes, ver. 0.19.0 (2014–).
[77] J. C. Slater, J. Chem. Phys. **41**, 3199 (1964).
[78] A. Kramida, Y. Ralchenko, J. Reader, and N. A. Team, NIST Atomic Spectra Database (version 5.12), Online (2024), accessed: Tue Nov 19 2024.
[79] S. V. Faleev, Y. Ferrante, J. Jeong, M. G. Samant, B. Jones, and S. S. Parkin, Phys. Rev. Appl. **7**, 034022 (2017), publisher: American Physical Society.
[80] L. Wollmann, S. Chadov, J. Kübler, and C. Felser, Phys. Rev. B **92**, 064417 (2015), publisher: American Physical Society.
[81] Y.-I. Matsushita, G. Madjarova, J. K. Dewhurst, S. Shallcross, C. Felser, S. Sharma, and E. K. U. Gross, J. Phys. D: Appl. Phys. **50**, 095002 (2017), publisher: IOP Publishing.
[82] T. Tadano and E. Xiao, NIMS computational heusler database (2025), the URL will be added after the paper is accepted.